

STATISTICAL FLUX TUBE PROPERTIES OF 3D MAGNETIC CARPET FIELDS

R. M. CLOSE, C. E. PARNELL, D. H. MACKAY and E. R. PRIEST

School of Mathematics and Statistics, University of St Andrews, North Haugh, St Andrews, Fife, KY16 9SS, Scotland (e-mail: robertc@mcs.st-and.ac.uk)

(Received 12 July 2002; accepted 25 September 2002)

Abstract. The quiet-Sun photosphere consists of numerous magnetic flux fragments of both polarities that evolve with granular and supergranular flow fields. These concentrations give rise to a web of intermingled magnetic flux tubes which characterise the coronal magnetic field. Here, the nature of these flux tubes is studied. The photosphere is taken to be the source plane and each photospheric fragment is represented by a series of point sources. By analysing the potential field produced by these sources, it is found that the distribution of flux tube lengths obtained by (i) integrating forward from positive sources and (ii) tracing back from negative sources is highly dependent on the total flux imbalance within the region of interest. It is established that the relation between the footpoint separation of a flux tube and its height cannot be assumed to be linear. Where there is a significant imbalance of flux within a region, it is found that fragments of the dominant polarity will have noticeably more connections, on average, than the minority polarity fragments. Despite this difference, the flux from a single fragment of either polarity is typically divided such that (i) 60–70% connects to one opposite-polarity fragment, (ii) 25–30% goes to a further 1 to 2 opposite-polarity fragments, and (iii) any remaining flux may connect to as many as another 50 or more other opposite-polarity fragments. This is true regardless of any flux imbalance within the region. It is found that fragments connect preferentially to their nearest neighbours, with, on average, around 60–70% of flux closing down within 10 Mm of a typical fragment. Only 50% of the flux in a quiet region extends higher than 2.5 Mm above the solar surface and 5–10% extends higher than 25 Mm. The fragments that contribute to the field above this height cover a range of sizes, with even the smallest of fragments contributing to the field at heights of over 50 Mm.

1. Introduction

Quiet-Sun photospheric regions are made up of an interwoven array of small magnetic fragments, termed the ‘magnetic carpet’ (Schrijver *et al.*, 1997). Magnetic flux is located in many fragments that form a network-like pattern which evolves with the supergranular convection. Supergranular cell sizes range from 13 Mm to 18 Mm in diameter (Hagenaar, Schrijver, and Title, 1997), and have a mean size of 15 Mm. The majority of the quiet-Sun flux originates in so-called ephemeral regions, which have a total absolute flux ranging from 2.6×10^{18} Mx to 407×10^{18} Mx (Hagenaar, 2001). They form clusters of fragments, whose total net flux is zero, and have a slight tendency to appear near the edges of supergranule cells (Wang, 1988). Hagenaar (2001) found the mean flux per ephemeral region to be around 11.3×10^{18} Mx, emerging at an average rate of 4.4×10^4 per day (averaged over



Solar Physics **212**: 251–275, 2003.

© 2003 Kluwer Academic Publishers. Printed in the Netherlands.

the entire Sun). With this rate of emergence, the magnetic field in the quiet Sun can be replaced every 14 hours.

The quiet Sun is dominated by network fragments, 90% of whose flux originates in ephemeral regions (Martin, 1990). Network regions (Martin, 1988) are typically found at sites of strong downflow, usually at the confluence of two or more supergranule cells. They have typical strengths of 10^{18} – 10^{19} Mx, and typical diameters of 1000–10 000 km. The remaining 10% of flux in the network fragments comes from the piling up of intranetwork fragments (Livingston and Harvey, 1975; Livi, Martin, and Wang, 1985; Martin, 1984, 1988, 1990; Wang, Zirin, and Shi, 1985; Wang and Shi, 1988; Wang and Zirin, 1988; Wang *et al.*, 1995; Zirin, 1985, 1987). These fragments have typical fluxes of 10^{16} – 10^{18} Mx (average 5×10^{16}). Intranetwork fragments are very small (diameter ~ 2000 km) and relatively shortlived, so as a consequence they have little impact on the outer atmosphere.

The typical behaviour of the photospheric magnetic flux in the quiet Sun can be described by four processes: (i) emergence – the appearance of new flux from below the photosphere; (ii) cancellation – the mutual loss of flux from opposite-polarity magnetic fragments; (iii) fragmentation – the break up of fragments into smaller ones and (iv) coalescence – the merging of fragments of the same sign to form a single larger fragment.

Recent models by Parnell (2001) and Simon, Weiss, and Title (2001) for the way in which the Sun's magnetic field distribution is created and maintained by ephemeral flux emergence, fragmentation, coalescence and cancellation build upon previous work by Schrijver *et al.* (1997) and Ballegoijen *et al.* (1998). Parnell estimated that the average emergence rate of new flux in the quiet Sun must lie between 6×10^{-2} and 10^{-5} Mx cm $^{-2}$ s $^{-1}$ in order to maintain an absolute flux density of 2.5–3 G. This requires a fragmentation rate of more than 12×10^{-5} s $^{-1}$ in order to agree with observations.

The motions of network elements force the coronal magnetic fields to interact in a complex way. The resulting interaction of intense photospheric flux tubes which have their footpoints rooted in the network may result in coronal heating through driven reconnection or braiding (Galsgaard and Nordlund, 1996).

Priest, Heyvaerts, and Title (2001) explored the formation and dissipation of current sheets on multiple separatrix surfaces (referred to as 'flux tube tectonics') and their effect on coronal heating. They found that simple relative motions (rather than complex braiding) of separate flux sources produce current sheets along the separatrices, which then dissipate rapidly by fast reconnection or in a turbulent manner. However, to understand better the connection between the photospheric magnetic field and the corona, and to investigate further heating mechanisms such as coronal tectonics, a good statistical understanding of the magnetic field above the photosphere is needed.

Schrijver and Title (2001) studied the statistical properties of the connectivity of field lines representing the magnetic field in the solar atmosphere by analysing the potential field over a source plane randomly sprinkled with 300 magnetic point

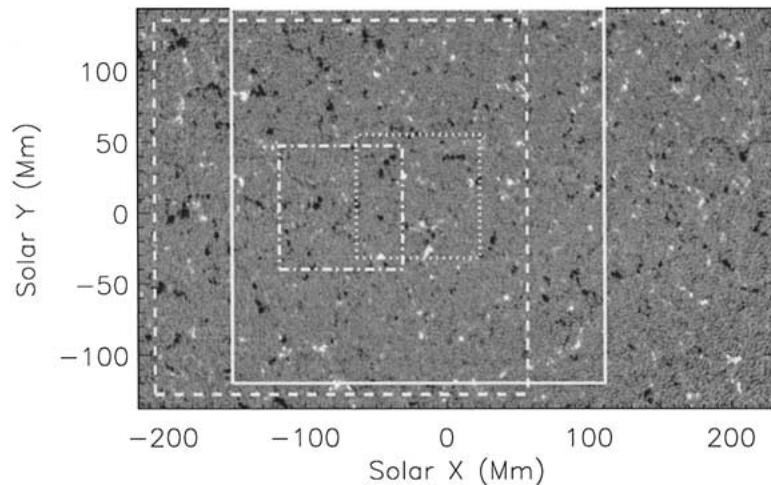


Figure 1. High-resolution MDI magnetogram of the quiet-Sun photosphere, taken on 13 June 1998. The *solid-line box* with the interior *dotted-line box* indicates the balanced region studied. The *dashed-line box* with the interior *dot-dashed line box* indicates the unbalanced region.

sources. By looking at 200 such realisations (in order to improve statistics), they found that each source connects to 1–12 opposite-polarity sources by field lines in the plane (typically 3–4), whilst the total number of opposite-polarity sources that a source is connected to by field lines both in and out of the plane ranges from 1 to 32, with an average of 8. They discovered a relation of approximately 1 null per source, with 91% lying in the source plane. One surprising result was that even the smallest sources frequently connect to many sources, with only a weak trend of stronger sources connecting to more sources. Despite the many connections, they found that 50% of the flux from a source connects to just one near source, 40% connects to another 2–6 near neighbours, with the remaining 10% connecting to as many as 25 other sources.

In this study, the aim is to explore the characteristics of flux tubes in a real quiet-Sun situation rather than the model situation of Schrijver and Title (2002). Using data from the Michelson Doppler Imager (MDI), the many flux fragments that are observed are represented by magnetic point sources. Rather than representing a fragment by a single point source with a strength equal to the total flux in that fragment, every pixel in the magnetogram belonging to a fragment is represented by an associated point source. As most fragments, especially larger ones, may consist of many point sources, this approach to modelling fragments better represents the geometry in each one. A potential field is constructed and, whilst performing a connectivity analysis similar to that of Schrijver and Title (2002), statistical properties of the flux tubes (such as lengths, heights and footpoint separations) are also studied. Furthermore, differences in results obtained from regions of varying flux imbalance are also assessed. Section 2 contains a detailed explanation of how the

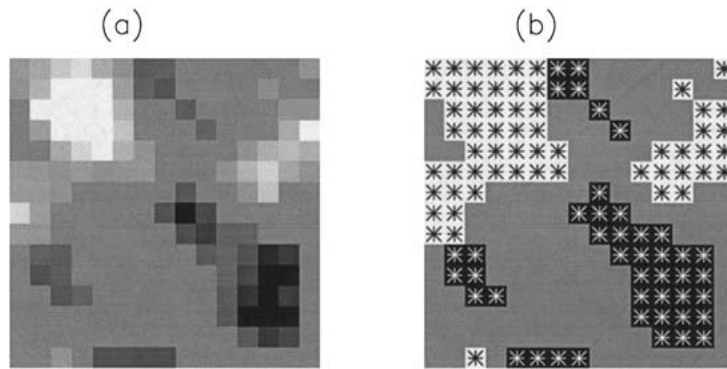


Figure 2. (a) Magnetogram image from the inner balanced region with noise removed. (b) Sketch of the point-source-per-pixel representation of the magnetogram. The *black stars* are positive point sources and the *white stars* are negative.

field is represented. Results are presented in three sections: Section 3 discusses properties of flux tubes, Section 4 details the connectivity between opposite polarity fragments, and Section 5 examines how individual fragments influence the field at varying heights.

2. Analysing the Magnetic Carpet

In order to study the properties of the magnetic carpet, high-resolution MDI magnetograms of the quiet Sun, observed near disk centre on 13 June 1998, are used. Before the analysis is performed, temporal noise in the data, which is largely due to 5-min oscillations, is reduced by averaging over 9 magnetograms spaced by 1 min. Furthermore, the resolution of the magnetogram is reduced by a factor of 2 in both the x and y directions by summing 2×2 groups of pixels. This helps reduce some of the spatial noise in the magnetogram.

To obtain information about the spectrum of flux tubes in the magnetic carpet, the flux in a magnetogram is represented by a series of point sources. Each macropixel is represented by a point source, which is placed in the centre of each pixel if the absolute flux density in the pixel is more than 20 Mx cm^{-2} . The flux of each source is set equal to the flux in the pixel it represents. Figure 2 shows a representation of a section of the magnetogram and the position of the point sources used. In order to consider the effects of choosing different regions with varying net flux, only a section of the magnetogram is used in the analysis; two subregions are specially selected to give preferred scenarios. In each case, a square, 300×300 macropixels in area, is selected with the subsequent analysis performed on a smaller inner square of just 100×100 macropixels so as to reduce greatly the bias of edge effects.

To calculate the field lines a potential field (i.e., a static field with $\nabla \cdot \mathbf{B} = 0$ and $\nabla \times \mathbf{B} = 0$) is used, and the solar surface is treated locally as a plane. The photosphere is taken to be the plane $z = 0$, and the solar atmosphere as the region $z > 0$. Since we only consider the plane $z \geq 0$ here, the sources are treated as points where flux passes through the $z = 0$ plane and are thus not isolated monopoles (which are not allowed since $\nabla \cdot \mathbf{B} = 0$). Approximating the magnetic field by a force-free field is valid when the plasma velocities are much smaller than the Alfvén speed. In such situations, the coronal field evolves through a series of equilibria. Although the field below the upper chromosphere is not force-free, much less current-free, here a potential field model is used for simplicity.

The potential field is obtained using the point-source Poisson solution, which gives the magnetic field $\mathbf{B}(\mathbf{r})$ at a given point $\mathbf{r} = x\hat{\mathbf{x}} + y\hat{\mathbf{y}} + z\hat{\mathbf{z}}$ by the following sum over all the sources:

$$\mathbf{B}(\mathbf{r}) = \sum_i \frac{\epsilon_i (\mathbf{r} - \mathbf{r}_i)}{|\mathbf{r} - \mathbf{r}_i|^3}, \tag{1}$$

where $\mathbf{r}_i = x_i\hat{\mathbf{x}} + y_i\hat{\mathbf{y}} + z_i\hat{\mathbf{z}}$ is the position of the i th source, with strength ϵ_i .

The field lines are calculated by numerically solving

$$\frac{dl}{|\mathbf{B}|} = \frac{dx}{B_x} = \frac{dy}{B_y} = \frac{dz}{B_z}, \tag{2}$$

using a classical fourth-order Runge–Kutta method of integration with a self-adjusting step-size. Field lines are calculated from starting points very close to the sources. Which sources are integrated from and how many field lines are calculated from each source is discussed later. Starting points for field lines are positioned on a hemisphere of radius δ centred on each source, where for a minimum source separation γ , say, we have $\delta \ll \gamma$.

If there are n field lines per source, then the hemisphere is split into p rings, with q segments per ring. This can be done in two ways such that there is always one field line positioned directly above the source and $n = pq + 1$ (Figure 3), or $n = pq$, such that no field line is started directly above the source (Figure 4).

Each starting point is calculated in such a way that each segment has the same area. In the case shown in Figure 3, where there is a field line directly above the source, the angles shown in the figure are given by

$$\theta_1 = \frac{\pi}{2}, \tag{3}$$

$$\theta_2 = \cos^{-1} \left(\frac{q}{1 + pq} \right), \tag{4}$$

$$\theta_i = \cos^{-1} ((i - 1) \cos \theta_2), \quad 2 < i \leq p, \tag{5}$$

$$\theta_{p+1} = \cos^{-1} (p \cos \theta_2), \tag{6}$$

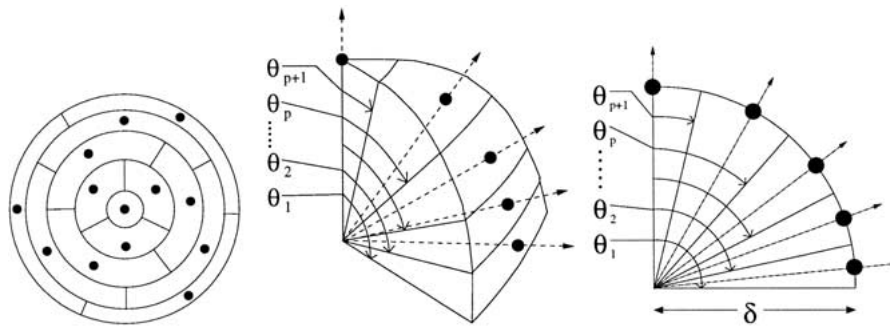


Figure 3. Example case showing starting points for $n = 13$; here $p = 4$ and $q = 3$, with one field line started directly above the source.

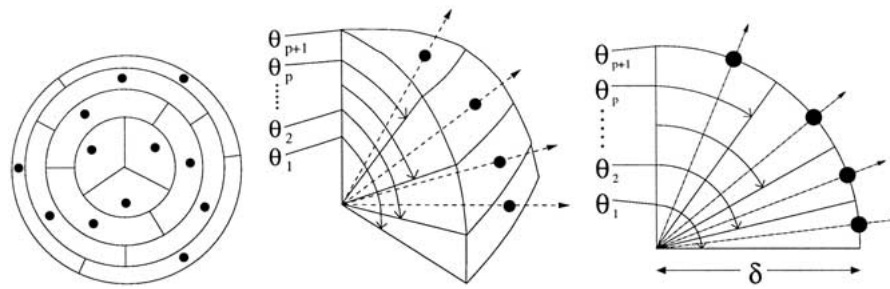


Figure 4. Example case showing starting points for $n = 12$; here $p = 4$ and $q = 3$, with no field line started directly above the source.

whereas when there is no field line directly above the source (Figure 4) the angles are

$$\theta_1 = \frac{\pi}{2}, \tag{7}$$

$$\theta_2 = \cos^{-1} \left(\frac{1}{p} \right), \tag{8}$$

$$\theta_i = \cos^{-1} ((i - 1) \cos \theta_2), \quad 2 < i \leq p, \tag{9}$$

$$\theta_{p+1} = 0. \tag{10}$$

In both cases, the angle ψ_i that the field line makes with respect to the vertical, with $\theta_{i+1} > \psi_i > \theta_i$, is given by

$$\psi_i = \cos^{-1} \left(\frac{1}{2} [\cos(\theta_{i+1}) + \cos(\theta_i)] \right). \tag{11}$$

The variables p and q are chosen such that the expression $p - q \geq 0$ is minimized. This also determines whether or not there will be a field line situated directly above the source. Each ring is offset from the one below it by an angle $2\pi/p$ so as to obtain a larger range in the directions in which the field lines point.

3. Flux Tube Characteristics

Two different regions, of size 300×300 macropixels (264×264 Mm), are picked from the full magnetogram, as shown in Figure 1, and the inner 100×100 (88×88 Mm) area is studied. The first region has a roughly balanced inner area (an exact flux balance is difficult to find), whereas the second region has a strong imbalance, with the ratio of positive flux to negative flux equal to 0.48 in the inner area. In both cases the entire flux inside the larger square is roughly balanced. The height of the domain in which the field lines are calculated is set at 264 Mm, equal to the horizontal size of the outer region.

For each of the two regions, m field lines are traced from each positive source of strength ϵ above 1.55×10^{17} Mx ($20 \text{ Mx cm}^{-2} \times \text{area of macropixel}$), with m equal to the integer part of ϵ/ϵ_1 (where $\epsilon_1 = 7.73 \times 10^{15}$ Mx = $1 \text{ Mx cm}^{-2} \times \text{area of macropixel}$), so that each field line represents the same amount of flux. This means that from each source a minimum of 20 field lines is traced. For each field line calculated, it is assumed that all the flux within the area it represents behaves in the same way. This is not strictly true, but, provided $\min(\epsilon) \gg \epsilon_1$, i.e., there are many field lines per source, it is a plausible assumption. Since in any continuous field a flux tube may be defined as being the surface made up of field lines that pass through a given curve, it is reasonable to refer to these field lines as flux tubes. Thus, the continuous coronal field is split into a set of magnetic flux tubes that each have flux ϵ_1 – hence, from a source of strength $\epsilon = 30\epsilon_1$, say, there would start 30 such flux tubes. Since field lines are allowed to leave the inner region, the distribution of lengths of field lines from both the polarities will not necessarily be the same, and so the process is repeated for field lines linking to the negative sources.

For each flux tube calculated, information is stored about (i) its footpoints, (ii) the strength of the fragments at these footpoints, (iii) the position of its maximum height, and (iv) its total length. For a random subset of the total number of flux tubes calculated, the coordinates of points along each flux tube are stored to produce field line plots. The results obtained from the flux tubes are then compared in order to deduce various properties of the magnetic carpet (Sections 3.1, 3.2, and 5).

In order to determine the connectivity of the region (discussed in Section 4), discrete fragments in the magnetogram are considered and information about the fragment to which each pixel belongs is stored and used to create connectivity matrices for the fragments of each polarity. Flux tubes that leave the domain through either the top or the outer sides are flagged and subsequently discarded in the analysis. Those that leave the inner box are followed to their footpoints in the outer region.

In the following discussion flux tubes that have been traced from positive fragments are referred to as ‘positive’ flux tubes, whilst those flux tubes traced from negative fragments are called ‘negative’ flux tubes.

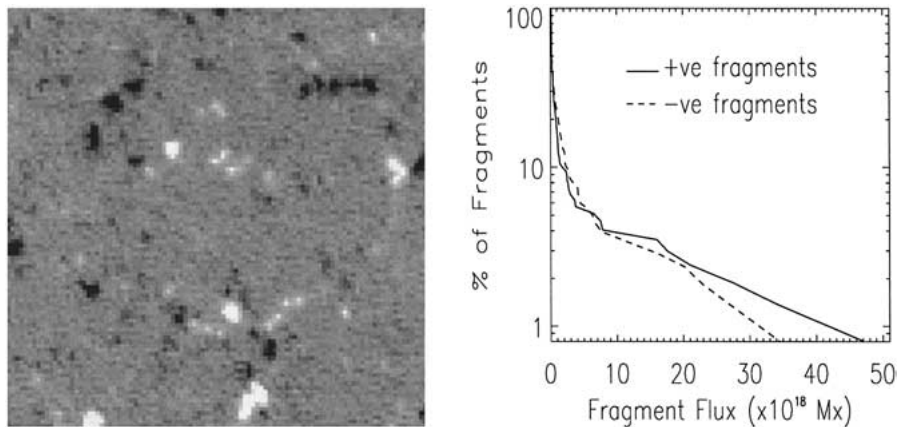


Figure 5. *Left*: the magnetogram image of the balanced 88×88 Mm inner region that is studied. *Right*: the percentage of fragments with flux over a given value is shown. The *dashed line* represents fragments with negative flux whilst the *solid line* represents fragments with positive flux.

3.1. A BALANCED INNER REGION

Within the balanced inner region (shown in Figure 5) there are 185 positive fragments which are represented by 816 point sources and 190 negative fragments represented by 802 point sources. The distribution of the strengths of these fragments is also shown in Figure 5 (*right*). For a given flux (x -axis), the y -axis gives the percentage of fragments with flux equal to or above this value. The total net flux is 24.5×10^{18} Mx in the inner region, corresponding to a mean field of 0.3 G, compared to the total absolute flux of 629×10^{18} Mx and total absolute mean field of 8.1 G. In the whole 300×300 macropixel region there are 2359 positive fragments represented by 7229 point sources and 1991 negative fragments represented by 7927 point sources.

The percentage of flux tubes with length greater than l is plotted in Figure 6(a) against length on a logarithmic axis. The dotted lines show that for flux tubes of both polarities, 50% are less than 14 Mm, whilst 25% are more than 35 Mm in length. Close inspection shows a mean flux tube length of around 35 Mm for the positive fragments and around 29 Mm for the negative fragments. This implies that the majority of flux from one quiet-Sun fragment closes within 1 or 2 supergranular cells. The two distributions are very similar, which is what one would expect for a balanced region. There is, however, a slight imbalance in flux in the region towards the positive polarity; the ratio of total positive flux to total negative flux is 1.08. This imbalance affects mostly the longer lengths of tubes, with the maximum positive flux tube length being far greater than the maximum negative flux tube length. Flux tubes with lengths up to 623.4 Mm are found by starting above positive fragments, whilst flux tubes of up to only 184.5 Mm can be traced back from negative fragments.

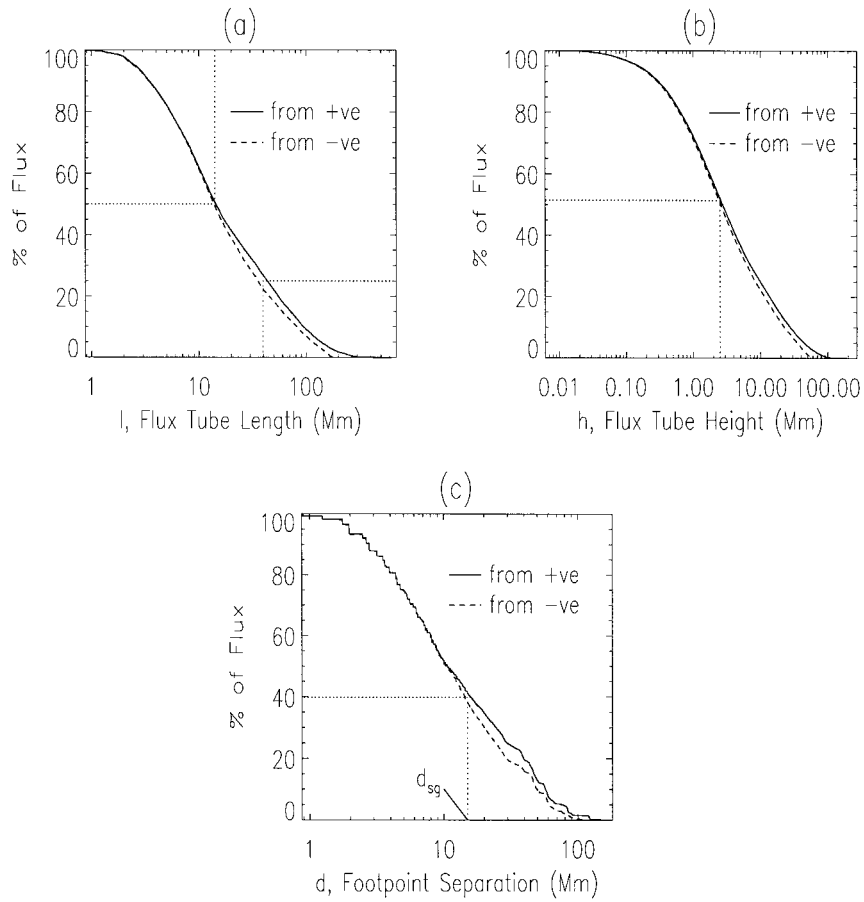


Figure 6. Percentage of flux tubes with (a) length greater than l , (b) height greater than h , and (c) endpoint separation greater than d . In all three plots the *solid lines* represent positive flux tubes and the *dashed lines* represent negative. Specific values are indicated by *dotted lines*, and d_{sg} indicates the diameter (15 Mm) of a typical supergranule cell.

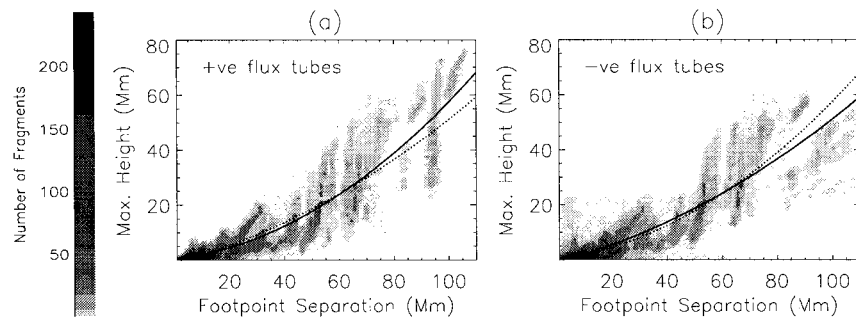


Figure 7. Contour plot of footpoint separation versus flux tube height for (a) positive flux tubes and (b) negative flux tubes. The lowest contour level is 1, with each subsequent contour level at 3 times the previous one. The *solid line* indicates the line fitted to the data in the plot and the *dotted line* is the line fitted to the data from the opposite polarity.

Naturally, some fragments, particularly those near the edge of the inner region, will be expected to connect to fragments outside the inner region. Here 21.7% of the positive flux from the inner region connects to the outer region, whilst 15.4% of the negative flux from the inner region connects to the outer region (7.5% of positive flux must connect outside the inner region due to the imbalance in flux).

Only 0.02% of flux tubes from positive fragments hit the upper boundary and only 0.02% hit the sides. None of the negative flux tubes hit the outer boundaries. It is not known whether these flux tubes represented genuine open flux or whether they would eventually connect to negative fragments in the absence of a boundary.

Another property of magnetic-carpet flux tubes worth investigating is their distribution of heights above the source plane. Figure 6(b) shows the percentage of flux tubes with maximum heights greater than h , against height. We are for simplicity modelling the field as a potential field, which fails near the photosphere (where gravitational effects enter) and sufficiently high in the corona (where inertial and pressure effects come into play), and also when there are Alfvénic plasma speeds or large enough currents present. Assuming the chromosphere to be of width 2.5 Mm (and accepting that taking the chromosphere and corona to be discretely separate layers is a naive assumption), it is found that 48% of the photospheric flux closes low down near the coronal base in the present approximation. Hence, only 52% of the total photospheric flux appears to reach into the corona for both positive and negative flux. Flux tubes from both polarities reach similar heights, with a mean height reached by the positive flux tubes of 9.5 Mm and a mean height for the negative flux tubes of 7.5 Mm. However, the maximum height reached by the closed positive flux tubes is 229.9 Mm, some four times higher than reached by the negative flux tubes, which is 59.5 Mm. This difference in maximum heights for the two polarities is due to the slight flux imbalance within the region.

Figure 6(c) shows a plot of the percentage of flux tubes with footpoints separated by more than a distance d . Around 41% of the flux from the positive concentrations extends over 15 Mm, the mean diameter of a typical supergranular cell (Hagenaar, Schrijver, and Title, 1997). If the larger ‘classical’ supergranular diameter of 32 Mm is considered (Simon and Leighton, 1964), then only 24% of the positive flux extends farther than this. These figures are similar for the negative concentrations, where it is found that 38% extend farther than 15 Mm and 19% farther than 32 Mm.

Figure 7 shows contour plots of footpoint separation against flux tube height for flux tubes of both polarities. It is clear, by merely glancing at the plots, that the maximum height of a flux tube increases as the footpoint separation is increased, which one would expect. Both plots have quadratic curves fitted to them, although the two curves vary quite significantly. This is mostly due to the slight imbalance within the region. The quadratic fitted to data for positive flux tubes has equation $0.0045d^2 + 0.12d + 0.4$, whilst for negative flux tubes the equation is $0.0023d^2 + 0.25d - 0.51$. These curves demonstrate that the relation between the footpoint separation and the maximum height of the flux tubes is not a linear one.

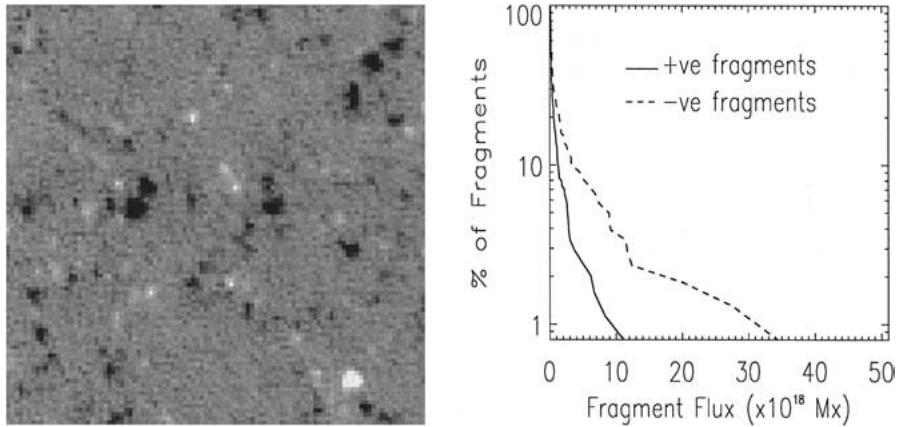


Figure 8. *Left*: the magnetogram image of the unbalanced 100×100 macropixel (88×88 Mm) inner region studied. *Right*: the percentage of fragments with flux over a given value is shown. The *dashed line* represents sources with negative strength whilst the *solid line* represents sources with positive flux.

3.2. AN UNBALANCED INNER REGION

To consider the effect of an unbalanced region of flux on the characteristics of potential flux tubes, a second region is investigated (the dashed line with dot-dashed box shown in Figure 1). For a given flux, the percentage of fragments with flux equal to or above this value is shown in Figure 8. Here the net flux is -186.5×10^{18} Mx in the inner region, corresponding to a mean field of -2.4 G, and there is roughly twice as much negative flux as positive flux. The total absolute flux is 526×10^{18} Mx, with a total absolute mean field of 6.8 G.

Within the unbalanced inner region studied here (shown in Figure 8), there are 222 positive fragments, represented by 608 point sources, and 192 negative fragments, represented by 930 point sources. The distribution of the strengths of these fragments is also shown in Figure 8. In the whole 300×300 macropixel region 2450 positive fragments are represented by 7543 point sources and 2019 negative fragments are represented by 8491 point sources. The analysis in the previous subsection is repeated for this unbalanced region.

Again, the percentage of flux tubes with lengths greater than l are plotted against length, (Figure 9(a)), with the x -axis logarithmic. The figure shows a substantial difference in the distributions of lengths of flux tubes from the two polarities for all flux tube lengths. As expected, flux tubes from the dominant (negative) polarity are generally longer than those from the minority (positive) polarity. The dotted lines show that for the positive flux tubes, 50% are longer than 9 Mm, whereas the negative flux tubes are generally longer with more than 70% having lengths of over 9 Mm and 50% with lengths over 23 Mm. For the positive flux tubes, 25% are over 17 Mm in length, whilst over 56% of negative flux tubes are over this length. Here the mean length of the positive flux tubes is only 15 Mm, whereas the mean length

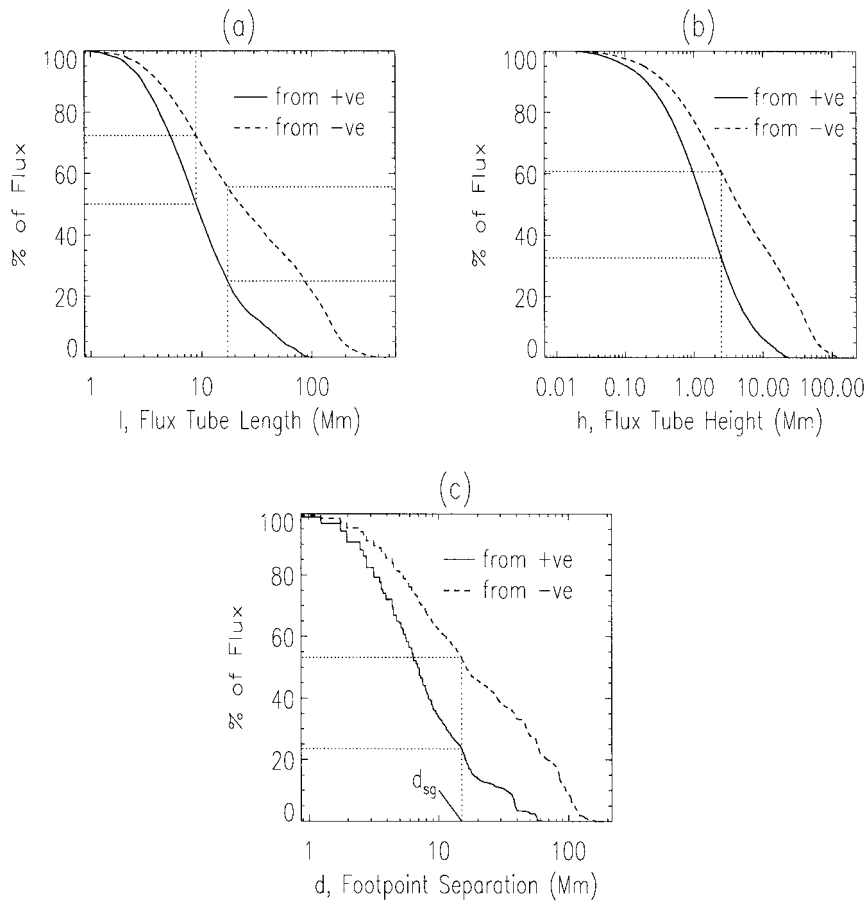


Figure 9. Percentage of flux tubes with (a) lengths greater than l , (b) heights greater than h and (c) footpoint separations greater than d . In all three plots the *solid line* represents flux tubes started from positive sources and the *dashed line* represents those started from negative sources. Specific values are indicated by *dotted lines*, and d_{sg} indicates the diameter of a typical supergranule cell.

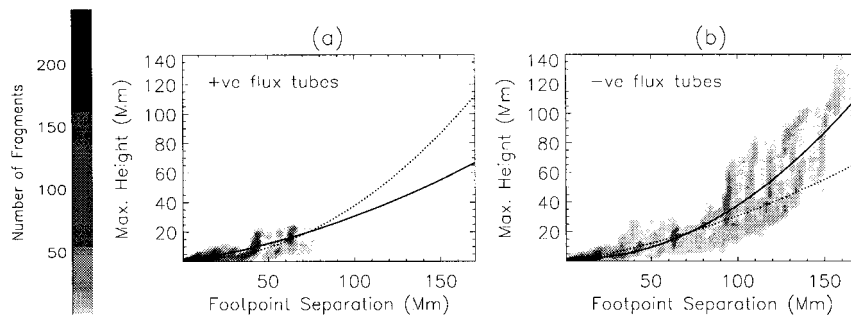


Figure 10. Contour plot of footpoint separation versus flux tube height for (a) positive flux tubes and (b) negative flux tubes. The lowest contour level is 1, with each subsequent contour level at 3 times the previous one. The *solid line* indicates the line fitted to the data in the plot and the *dashed line* represents the opposite polarity flux tubes.

of the negative flux tubes is 55 Mm. This large difference in mean flux tube length is due to the flux imbalance in the inner region (positive/negative flux ≈ 0.48), which results in much of the negative flux connecting to fragments outwith the inner area. The maximum length of the positive flux tubes is 100 Mm, whereas the maximum length of the negative flux tubes is far greater at 499 Mm. Here it is found that only 3.4% of the positive flux connects to fragments outside the inner region, whereas this figure is 54.0% for negative fragments. This is not surprising due to the flux imbalance. As a consequence of the flux imbalance 52.4% of the negative flux from the inner area must connect to the outer region. Of all the field lines calculated, none from the positive fragments nor the negative fragments in the inner region hit the outer boundaries.

For this region, it is found that the mean height reached by flux tubes from the positive fragments is 2.8 Mm, with a maximum height reached of 24.2 Mm. In contrast, flux tubes from negative fragments have a mean height of 15 Mm and a maximum height reached of 183 Mm. This is clearly illustrated in the plots showing the distribution of flux tube heights in Figure 9(b). Taking the chromosphere to be of width ~ 2.5 Mm, and bearing in mind the assumptions concerning the validity of this model previously discussed for the balanced region, results in 33% of flux tubes from positive fragments reaching coronal heights, whereas for flux tubes from negative fragments this figure is almost double at 61%.

Around 23% of the flux from the positive fragments extends out farther than the 15 Mm diameter of a typical supergranular cell. More than double that, 53%, of flux from negative fragments extends farther than this length. However, taking the diameter of a supergranule to be 32 Mm results in values of 10% and 37%, respectively, of the positive and negative flux tubes extending farther than a supergranule (Figure 9(c)).

Figure 10 shows slightly different behaviour for the flux tubes in the unbalanced region than in the balanced region shown in Figure 7. It is still generally true that the larger the footpoint separation, the greater the maximum height of the flux tube. However, now the curves fitted to the data vary much more, although this is likely to be because the range of footpoint separations and maximum heights is much smaller for the positive flux tubes than the negative flux tubes. The quadratics now have equations $0.0013d^2 + 0.18d + 0.03$ for the positive flux tubes and $0.004d^2 - 0.061d + 2.1$ for negative flux tubes. The negative quadratic appears to be a reasonable fit to the positive data and so the imbalance does not appear to have changed the relation between footpoint separation and maximum height of the flux tubes. These curves again show that the relation between footpoint separation and flux tube height cannot be assumed to be a linear one.

The contrast in flux tube lengths obtained for this imbalanced region compared to the previous balanced region demonstrates that the flux tube length spectrum for a given region is highly dependant on the flux balance within that region. It is most likely that longer flux tubes than those found here may be obtained in other regions observed within quiet-Sun areas, although, as the size of the region

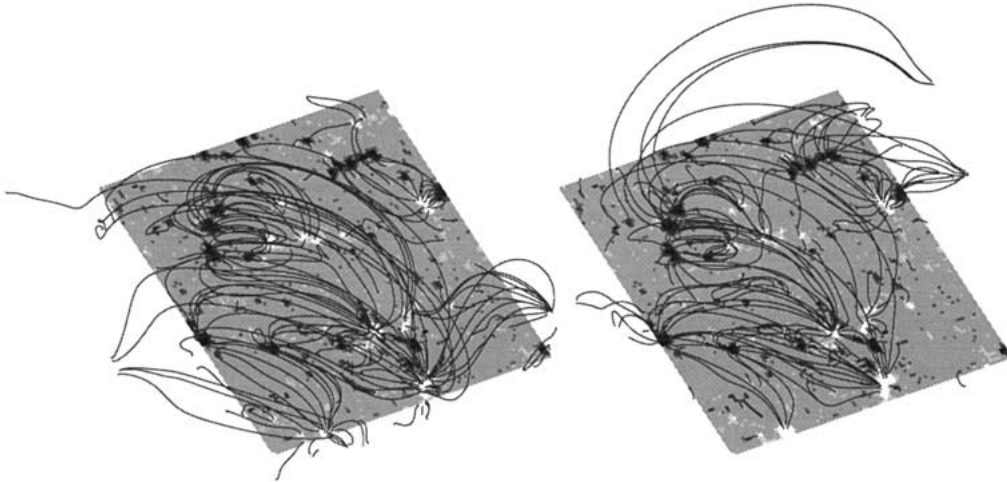


Figure 11. Magnetogram of the balanced region magnetogram together with a subset of the field lines calculated from the positive sources (*left*) and the negative sources (*right*).

examined is increased, the maximum possible imbalance will decrease. In a given region there will be areas that have a greater local imbalance than others, so that the maximum flux tube length possible from fragments within a region will depend on the balance between the size of the flux imbalance and the area over which the imbalance occurs.

4. Connectivity

Having looked at the characteristics of flux tubes themselves, now let us consider the individual fragments and their connections. By considering connected macropixels of the same polarity to be a fragment, matrices of the connectivity from each fragment are calculated and connectivity properties are thus deduced. In the following discussion, the number of negative fragments that an individual positive fragment connects to are termed ‘positive’ connections, whilst the number of positive fragments that an individual negative fragment connects to are termed ‘negative’ connections.

4.1. BALANCED REGION

For the balanced region studied, the field line plots in Figure 11 show fairly similar behaviour for the flux tubes from both the positive fragments and the negative fragments. The flux tubes in both plots are comparable in length, with roughly the same number of flux tubes connecting outwith the inner region in both cases.

The maximum number of positive connections is 65, whilst the maximum number of negative connections is 38. For fragments of both polarities the mean number

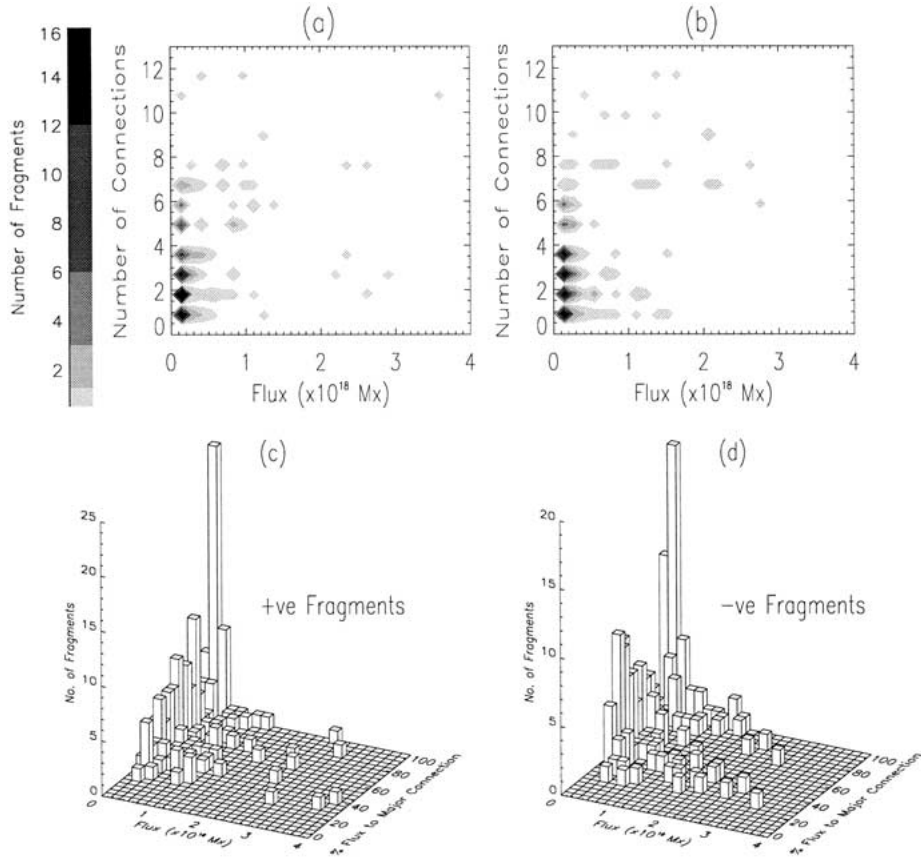


Figure 12. Contour plots showing the number of fragments to which a fragment of given flux connects for (a) positive fragments and (b) negative fragments. The lowest contour level is 1, with each subsequent contour level set at twice the previous one. Also shown are 3D bar graphs of fragment flux versus percentage flux to major connection for (c) positive fragments and (d) negative fragments.

of connections is ~ 5 . Figures 12(a) and 12(b) show that connectivity for fragments of both polarities is similar, with many small fragments (flux $< 10^{18}$) having 1–7 connections. There is a slight trend for larger fragments to have more connections, although there is much scatter in the plots. Figures 12(c) and 12(d) show that the flux from the smaller fragments of both polarities often connects almost entirely to a single opposite polarity fragment. In some cases, though, as little as 20% of the flux from the smallest of fragments connects to a single fragment. This implies a minimum of 5 connections from such fragments. Figure 13(a) shows that the 10% of positive fragments with the most connections have 8 connections or more, whilst the largest 10% of negative fragments have 10 connections or more. In Figure 13(b), each set of opposite polarity fragments that are connected to a single fragment are sorted in decreasing order with respect to the amount of connected flux. The stars (diamonds) denote the range of possible amounts of flux connected

for the various positive (negative) fragments. The solid (dashed) lines give the mean flux connected to each fragment, again for the positive (negative) fragments. The two lines almost lie upon one another. From this it can be seen that the mean flux linked to the first (major) connection is 68% for both polarities. However, the range of possible flux connected is large, ranging from 15–100%. Up to 25% of the remaining flux connects to another 1–2 fragments, while the remaining 7% of flux connects to up to as many as 62 fragments for positive fragments and 34 fragments for negative ones (only the first 10 fragments are shown in Figure 13(b)).

The scatter plot in Figure 13(c) shows that, for a given fragment, the mean distance to connected opposite polarity fragments is largely independent of the fragment flux. Smaller fragments connect, on average, to fragments distributed over a wide range of distances. However, as the fragment flux is increased, this range decreases, with the largest fragments connecting mostly to opposite polarity fragments at relatively large distances. There is, perhaps unsurprisingly, a tendency for fragments to connect preferentially to their nearest neighbours. Indeed, 60–66% of flux closes, on average, within 9 Mm of a fragment. Although there is an average of ~ 2 connected fragments within this radius, the figures indicated suggest (by comparison with Figure 13(d)) that the connection with the second largest amount of flux does not necessarily lie within 9 Mm of the fragment in question. For this balanced region, the plots for both polarities of fragments are essentially the same.

Schrijver and Title (2002) found that strong fragments could connect to over 30 other opposite polarity fragments and, using an expectation value of one fragment per area of order $A \approx 2 \times 10^8 \text{ km}^2$ (Schrijver *et al.*, 1997), they estimated that direct connections fanned out over a radius of order $r = (30 \times 2 \times A/\pi)^{1/2} \approx 60 \text{ Mm}$.

The expectation value is found here to be instead one fragment per area of $A \approx 1.6 \times 10^7 \text{ km}^2$. Using this value, an estimate to the number of fragments within reach of a particular positive (negative) fragment is given by $I_n \pi r^2 / A$ ($I_p \pi r^2 / A$), where I_n (I_p) is the ratio of the total negative (positive) flux to the total flux of both polarities and r is the distance over which direct connections occur. This is essentially the inverse of the calculation by Schrijver and Title (2002).

The positive flux tubes have a mean footpoint separation of 22 Mm, so on average, taking I_n to be 0.48, the flux from a typical fragment extends out over an area containing ~ 44 fragments. For the maximum footpoint separation of 156 Mm, this figure is 2297 fragments. For negative fragments, with I_p equal to 0.52 and a mean footpoint separation of 19 Mm, flux extends out over an area containing ~ 36 fragments. For the maximum endpoint separation of 118 Mm, this figure is 1411 fragments. For such numbers of connections to be observed, this would require that (i) the field is sufficiently sampled and (ii) there are enough opposite polarity fragments to provide the connections. Here we have 7672 flux tubes traced from the largest positive fragment and 4818 from the largest negative fragment, which is indeed enough to show up all the connections. Although there are 2359 positive fragments in the whole region, which is enough to provide the connections for the

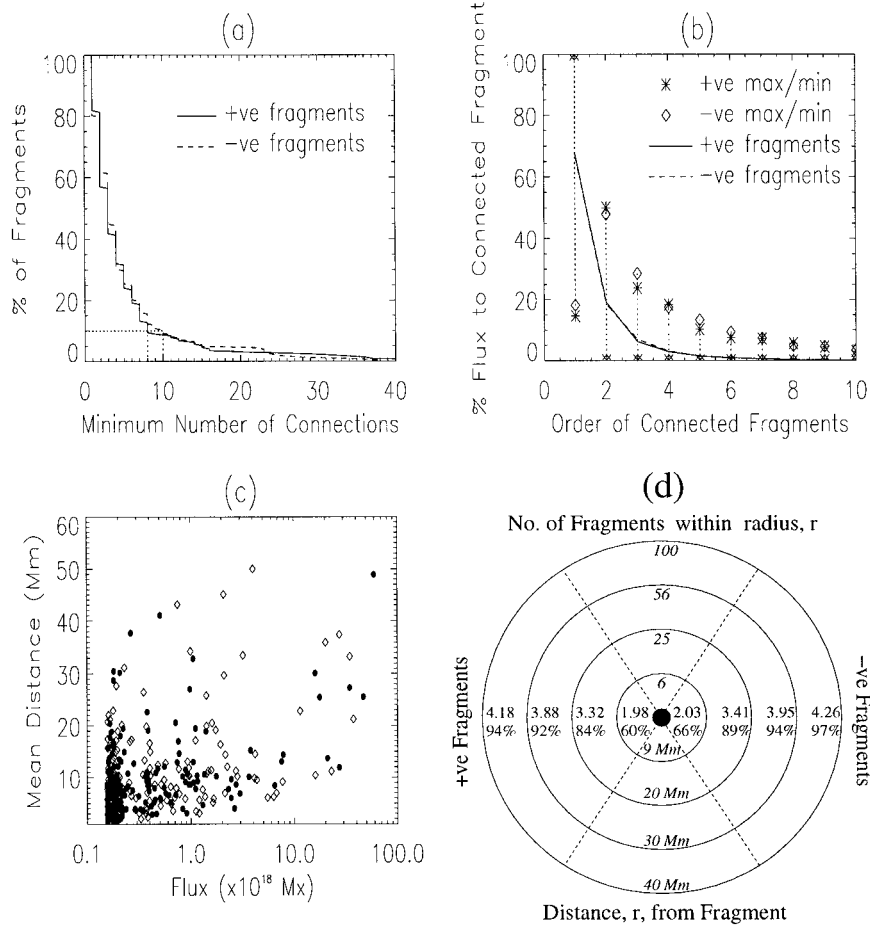


Figure 13. (a) Percentage of fragments against minimum number of connections of that fragment. (b) Mean proportion of flux for each fragment to which a given fragment connects. (c) Scatter plot of fragment flux versus the mean of the distances to connected fragments for positive fragments (filled circles) and negative fragments (diamonds). (d) Diagram showing distribution of flux and connections for both a typical positive fragment (left) and a typical negative fragment (right), against radius, r . The percentages show, as an average, the total amount of closed flux within a given radius, whilst the numbers show the average number of connected fragments within the given radius. The figure giving the number of fragments within a radius only includes those of the opposite polarity.

negative fragments, there are only 1991 negative fragments. Thus, the maximum is 1991 connections for the largest positive fragment. Since the values for the number of connections found are much lower than these estimates, this indicates that fragments do not connect to all the fragments within their dome of influence, and that they do not tend to be situated in the centres of their dome of influence (inside their separatrix dome), but rather near the edge, and so assuming a full circle around the fragments is unrealistic.

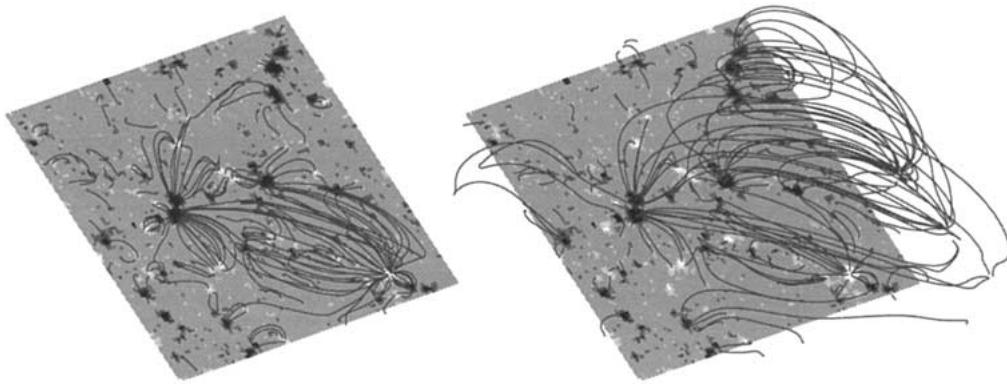


Figure 14. Magnetogram of the unbalanced region together with a subset of the field lines calculated from the positive sources (*left*) and the negative sources (*right*).

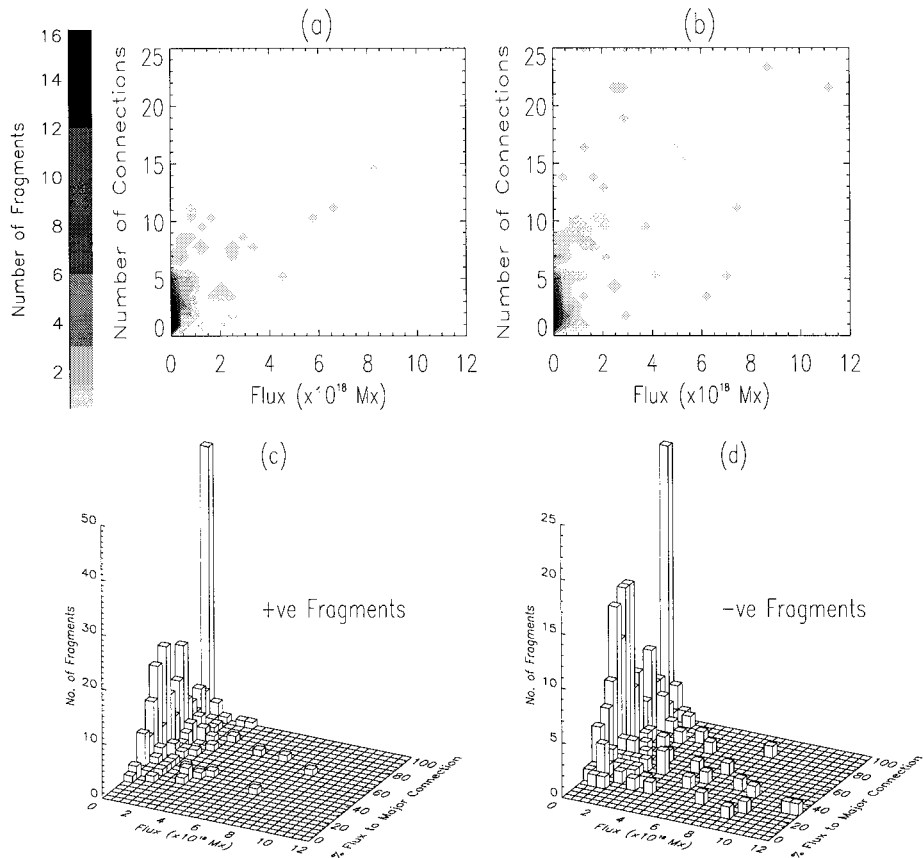


Figure 15. Contour plots showing the number of fragments to which a fragment of given flux connects for (a) positive fragments and (b) negative fragments. The lowest contour level is 1, with each subsequent contour level set at twice the previous one. Also shown are 3D bar graphs of fragment flux versus percentage flux to major connection for (c) positive fragments and (d) negative fragments.

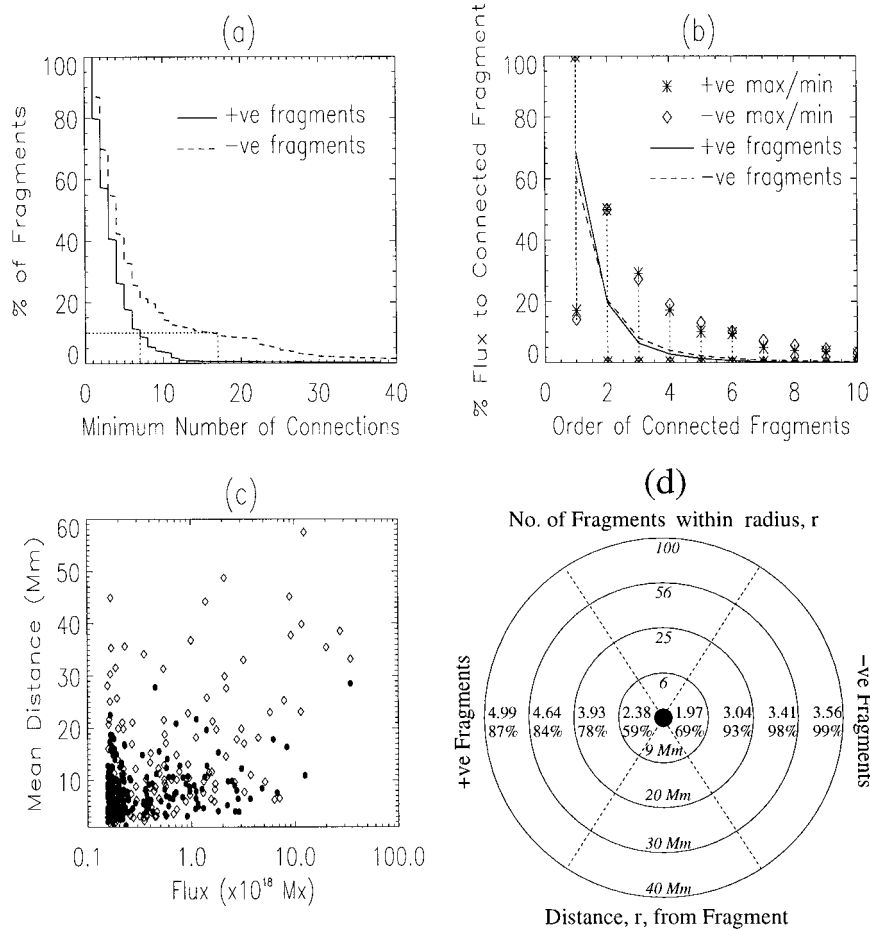


Figure 16. (a) Percentage of fragments against minimum number of connections from that fragment. (b) Mean proportion of flux for each fragment to which a given fragment connects. (c) Scatter plot of fragment flux versus the mean of the distances to connected fragments for positive fragments (filled circles) and negative fragments (diamonds). (d) Diagram showing distribution of flux and connections for both a typical positive fragment (left) and a typical negative fragment (right), against radius, r . The percentages show, as an average, the total amount of closed flux within a given radius, whilst the numbers show the average number of connected fragments within the given radius. The figure giving the number of fragments within a radius only includes those of the opposite polarity.

4.2. UNBALANCED REGION

The contrast between the two field line plots in Figure 14 for the unbalanced region demonstrate how the flux from the negative fragments dominates the field. As a result of the imbalance of flux in favour of the negative polarity, many of the negative flux tubes must close outside the inner region, which is clearly shown. Hardly any positive flux tubes close outside the inner region, which is also reflected in the plot.

From the positive fragments there are at most 38 connections, with a mean of 3.7 connections. For the negative fragments, these values are roughly double, with a maximum number of connections of 75 and a mean of 6.7 connections. The contour plots in Figures 15(a) and 15(b) further emphasise this difference, showing clearly that negative fragments tend to have substantially more connections. There is again a definite trend for stronger fragments of both polarities to have more connections, whilst many of the fragments of strength less than 10^{18} Mx have 1–5 connections. Figures 15(c) and 15(d) show again that the bulk of the flux from a single fragment frequently connects to only a few other fragments. It is mostly the larger fragments that have their flux distributed more evenly over a greater number of sources. Figure 16(a) shows that the distribution of connections for fragments of the two polarities differ greatly. The 10% of positive fragments with most connections have a minimum of 7 connections or more, whereas for the negative fragments the top 10% with the most connections have 17 connections or more. This demonstrates that the dominant polarity in an unbalanced region has more connections than the minority polarity, as one would expect. Despite this, however, Figure 16(b) shows that the mean flux to the major connection for both polarities lies around 65%, with up to 27% of flux connecting to another 1 or 2 fragments and the remaining $\sim 8\%$ of flux connecting to up to a possible 34 further fragments for the positive fragments and 71 fragments for the negative fragments.

For a given fragment, the mean distance to connected fragments is again effectively independent of the fragment flux (Figure 16(c)). The positive (minority) polarity fragments connect on average to negative fragments over a shorter range than the negative fragments. There is much evidence from Figure 16(d) for both polarities suggesting that a fragment connects preferentially to its nearest neighbours. 59–69% of flux closes, on average, within 9 Mm of a fragment. Again, the figures shown suggest that the connection with the second largest amount of flux does not necessarily lie within 9 Mm of the fragment in question.

5. Properties of Fragments

So far the distribution of flux tube heights above the source plane has been described, so now we turn to the properties of the fragments that produce these flux tubes. Although one might expect only the larger fragments to contribute flux to the field at larger heights, it is found instead that at a given height the field is comprised of flux from fragments over a wide range of sizes.

5.1. BALANCED REGION

The scatter plot in Figure 17(a) shows the maximum heights reached by flux from fragments of both polarities. The behaviour is similar for both positive and negative fragments; only the flux from smaller fragments closes entirely at low heights, although many small fragments have some proportion of their flux reaching relatively

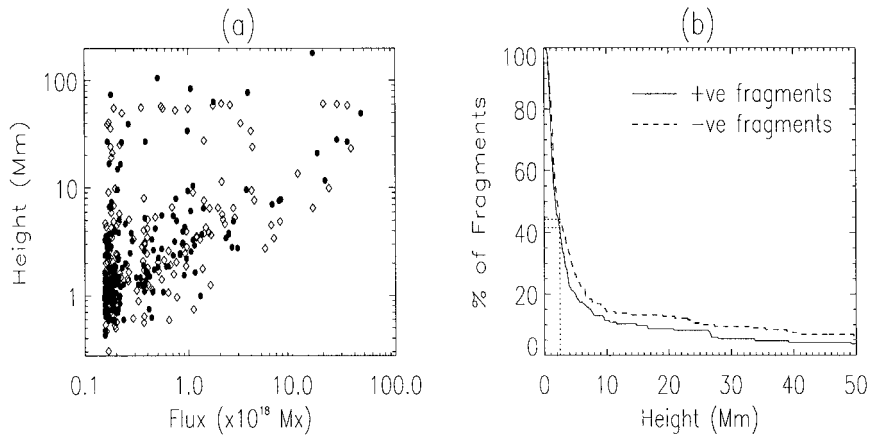


Figure 17. (a) Scatter plots showing fragment flux versus maximum height reached by flux from that fragment for positive fragments (*filled circles*) and negative fragments (*diamonds*). (b) Plot showing, for a given height, the percentage of fragments with flux reaching that height (or higher).

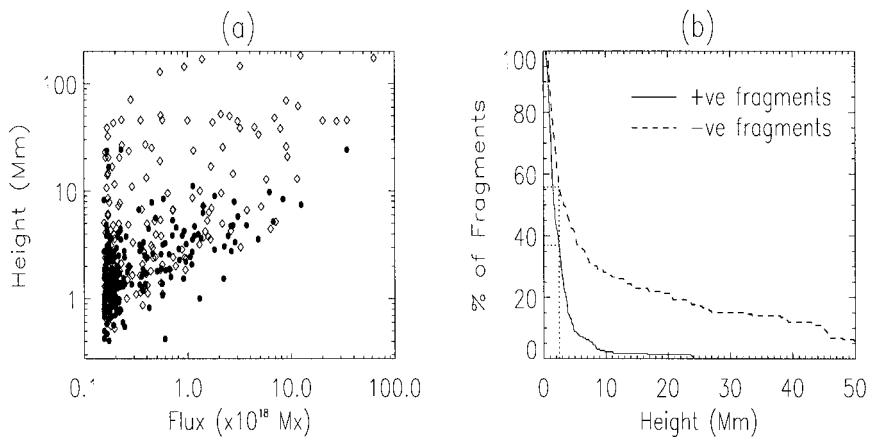


Figure 18. (a) Scatter plots showing fragment flux versus maximum height reached by flux from that fragment for positive fragments (*filled circles*) and negative fragments (*diamonds*). (b) Plot showing, for a given height, the percentage of fragments with flux reaching that height (or higher).

large heights. The fact that in the lower-right triangle of the plot there are no points means that larger fragments will always have some of their flux reaching the larger heights. Figure 17(b) shows that the 52% of flux from fragments of both polarities that reaches coronal heights (i.e., above 2.5 Mm) is produced by around 43% of the fragments. Thus, flux from 57% of all fragments does not reach the corona. Fragments that close entirely under 2.5 Mm are small (under 2×10^{18} Mx), each accounting for under 1% of the total unsigned flux within the region.

5.2. UNBALANCED REGION

The graph in Figure 18 showing the maximum heights reached by flux from fragments of both polarities in the unbalanced region displays the same characteristics as fragments in the balanced region, with the figures adjusted accordingly (since positive flux tubes reach a mean height of only 2.8 Mm compared to 24.2 Mm for negative flux tubes). Again, only the flux from the smaller fragments may close entirely at relatively low heights, with larger fragments always having some proportion of their flux reaching larger heights. Figure 18(b) shows that the 61% of positive flux that reaches a height of 2.5 Mm or over is produced by 56% of the negative fragments, whilst the 33% of positive flux that exceeds this height is produced by 37% of the positive fragments. Positive fragments whose entire flux closes below 2.5 Mm have flux under 3×10^{18} Mx (less than 2% of the total positive flux in the inner region), whilst negative fragments whose entire flux closes below 2.5 Mm have flux less than 1×10^{18} Mx (less than 1% of the total negative flux).

6. Conclusions

This study of flux tube characteristics and fragment connections from an MDI magnetogram represented by a series of point sources (for each pixel over 20 G) and extrapolated into the corona using a potential field has revealed several interesting properties. The distribution of lengths of flux tubes determined by examining both the flux that leaves the positive fragments and the flux that closes down on the negative fragments is highly dependant on the total flux imbalance within the region of interest. Any flux imbalance will be mainly noticeable at the higher end of the distributions for both polarities. Even the quiet-Sun regions studied here are found to produce flux tubes that are 100 Mm long. Indeed, roughly 10% of the flux in both cases is contained in such loops. Furthermore, it is found that much of the flux from the quiet Sun is contained in low-lying flux tubes. This means that only 50% of the flux that threads the surface of the Sun extends further than 2.5 Mm above the surface and only 5–10% extends further than 25 Mm, as shown in Figure 19. Thus, assuming a minimum coronal height of 2.5 Mm, all these low-lying loops never reach the corona. Hence, the magnetic field strength in the corona does not just fall off as $1/R^3$ in accordance with the expansion of the volume into which it is extending, but it falls off much faster due to the closure of magnetic field at lower heights. Analysis of the footpoint separation of the flux tubes shows that about 15% of the total flux connects to fragments that are within 5 Mm of each other. That is, they are connected to fragments that are probably in the same supergranular lane as themselves.

Typically 50% of the fragments contribute flux to the field above 2.5 Mm. Fragments whose entire flux closes before this height are small (flux $< 2 \times 10^{18}$ Mx), although many smaller sources have some of their flux reaching larger heights.

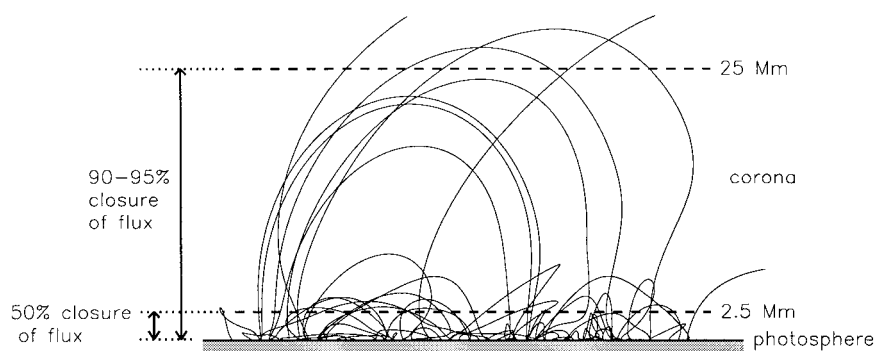


Figure 19. Side view of a typical 3D magnetic carpet field: 50% of flux closes below 2.5 Mm, whilst 5–10% of flux extends above 25 Mm.

Larger fragments, in contrast, will always have some of their flux reaching relatively large heights.

For a balanced region, similar positive fragments and negative fragments will have, on average, the same number of connections. Here a mean of 5 connections per fragment was found. For an unbalanced region, fragments of the dominant polarity will have more connections, on average, than those from the minority polarity. Here the total flux of both polarities varied by a factor of ~ 2 and fragments of the dominant polarity had around twice as many connections, approximately 7, as the minority polarity concentrations.

Despite the fact that flux from a particular fragment may be expected to extend out over an area containing many opposite polarity fragments, the results obtained here show that the majority of these will not connect to the fragment in question. There are two reasons for this. Firstly, the estimates in this study assume that a fragment is situated in the centre of its dome of influence, whereas in practice it is more likely to be situated nearer the edges. Indeed, the area over which flux from a given fragment extends is also highly unlikely to be circular. Secondly, many fragments within the area often connect entirely to other fragments. Thus, when calculating the field, the contribution from such fragments will cancel with the flux from the fragments that it connects to, resulting in many neighbouring fragments being effectively 'hidden' from the given source. So, despite the multitude of fragments, many features of the topology of a field produced by a small set of sources will be present here. The field produced by the many quiet-Sun fragments may be considered, to a certain extent, to be made up of a superposition of the fields produced by many low-order systems of only a small number of fragments.

The connectivity analysis performed here is in good agreement with the results obtained by Schrijver and Title (2002). Both studies show, in particular, that:

(1) Although there is a trend, which shows up in all cases studied here, for stronger fragments to be connected to more opposite-polarity fragments, there is at any fragment strength a wide range of possible connections. Even the smallest frag-

ments can have up to 7 connections, and the largest fragments can have between 10 and 60 connections.

(2) Fragments show, perhaps unsurprisingly, a preference towards connecting to nearby opposite-polarity fragments. On average, roughly 60–70% of flux from a given fragment connects to an opposite polarity fragment within a 9 Mm radius. However, some connections may span several supergranular diameters.

(3) Despite the vast number of possible connections, the bulk of the flux from a typical fragment is here found to be divided such that (i) 60–70% connects to one opposite polarity fragment (ii) 25–30% goes to a further 1 to 2 opposite-polarity fragments and (iii) any remaining flux may connect to as many as another 50 or more other opposite-polarity fragments. The figures obtained by Schrijver and Title (2002) are (i) 50% of flux goes to the major connection, (ii) 40% goes to another 2–6 near fragments, and (iii) the remaining 10% may connect to up to 25 further fragments.

(4) There is evidence for nesting of domes of connectivity. Schrijver and Title (2002) observe this directly, whereas in this study it is inferred from knowledge of the distance over which direct connections occur.

Differences in exact figures will be due to the different methods of modelling the quiet-Sun photospheric fragments.

From this study it can be seen that potential field extrapolation and knowledge of connectivity within a region may provide useful information as to which fragments are related to events observed higher up in the solar atmosphere.

Acknowledgements

The authors would like to thank both C. J. Schrijver and the referee, B. T. Welsch, for their helpful comments regarding improvements to this paper. We must thank the Particle Physics and Astronomy Research Council for financial support.

References

- Galsgaard, K. and Nordlund, Å.: 1996, *J. Geophys. Res.* **101**, 13445.
Hagenaar, H. J.: 2001, *Astrophys. J.* **555**, 448.
Hagenaar, H. J., Schrijver, C. J., and Title, A. M.: 1997, *Astrophys. J.* **988**, 481.
Livi, S. H. B., Martin, S. F., and Wang, H.: 1985, *Australian J. Phys.* **38**, 855.
Livingston, W. C. and Harvey, J. W.: 1975, *Bull. Amer. Astron. Soc.* **7**, 346.
Martin, S. F.: 1984, in S. L. Kleid (ed.), *Proc. Symp. on Small-scale Dynamical Processes in Quiet Sun Stellar Atmospheres*, National Solar Observatory, Sacramento Peak, NM, p. 30.
Martin, S. F.: 1988, *Solar Phys.* **117**, 243.
Martin, S. F.: 1990, in J. O. Stenflo (ed.), *Solar Photosphere: Structure, Convection and Magnetic Fields*, Proceedings of the 138th Symposium of International Union, Kiev, U.S.S.R., Kluwer Academic Publishers, Dordrecht, p. 129.
Parnell, C. E.: 2001, *Solar Phys.* **200**, 23.

- Priest, E. R., Heyvaerts, J. F., and Title, A. M.: 2002, *Astrophys. J.* **576**, 000.
- Schrijver, C. J. and Title, A. M.: 2002, *Solar Phys.* **207**, 223.
- Schrijver, C. J., Title, A. M., Van Ballegoijen, A. A., Hagenaar, H. J., and Shine, R. A.: 1997, *Astrophys. J.* **487**, 424.
- Schrijver, C. J., Title, A. M., Harvey, K. L., Sheeley, N. R., Wang, Y. M., Van Den Oord, G. H. J., Shine, R. A., Tarbell, T. D., and Hurlburt, N. E.: 1998, *Nature* **394**, 152.
- Simon, G. W. and Leighton, R. B.: 1964, *Astrophys. J.* **140**, 1120.
- Simon, G. W., Weiss, N. O., and Title, A. M.: 2001, *Astrophys. J.* **561**, 427.
- Title, A. M.: 2000, *Phil. Trans. R. Soc. London* **A358**, 657.
- van Ballegoijen, A. A., Nisenson, P., Noyes, R. W., Löfdahl, M. G., Stein, R. F., Nordlund, Å., and Krishnakumar, V.: 1998, *Astrophys. J.* **435**, 509.
- Wang, H.: 1988, *Solar Phys.* **115**, 205.
- Wang, H. and Shi, Z.: 1988, *Acta Astron. Sinica* **29**, 48.
- Wang, H. and Zirin, H.: 1988, *Solar Phys.* **115**, 205.
- Wang, H., Zirin, H., and Shi, Z.: 1985, *Solar Phys.* **98**, 241.
- Wang, J., Wang, H., Tang, F., Lee, J. W., and Zirin, H.: 1995, *Solar Phys.* **160**, 277.
- Zirin, H.: 1985, *Australian J. Phys.* **38**, 961.
- Zirin, H.: 1987, *Solar Phys.* **110**, 101.